



CERN-EP-2023-227
LHCb-DP-2023-002
09th October 2023

Helium identification with LHCb

LHCb collaboration[†]

Abstract

The identification of helium nuclei at LHCb is achieved using a method based on measurements of ionisation losses in the silicon sensors and timing measurements in the Outer Tracker drift tubes. The background from photon conversions is reduced using the RICH detectors and an isolation requirement. The method is developed using pp collision data at $\sqrt{s} = 13$ TeV recorded by the LHCb experiment in the years 2016 to 2018, corresponding to an integrated luminosity of 5.5 fb^{-1} . A total of around 10^5 helium and antihelium candidates are identified with negligible background contamination. The helium identification efficiency is estimated to be approximately 50% with a corresponding background rejection rate of up to $\mathcal{O}(10^{12})$. These results demonstrate the feasibility of a rich programme of measurements of QCD and astrophysics interest involving light nuclei.

Submitted to JINST

© 2023 CERN for the benefit of the LHCb collaboration. CC BY 4.0 licence.

[†]Authors are listed at the end of this paper.

1 Introduction

The observation of antihelium in Cosmic Rays (CR) could be a signature for physics beyond the standard model, such as dark matter annihilation [1] or the existence of antimatter domains in space [2]. The AMS-02 experiment [3] aboard the International Space Station (ISS) has reported several antihelium candidates of unclear origin [4]. Light nuclei can also be produced in interactions of CR with the interstellar medium via coalescence of secondary baryons, where the CR and the interstellar gas are mostly protons and around 10% helium [5]. The coalescence of antibaryons into antinuclei has been studied at colliders, for example at the LHC in pp and PbPb collisions (ALICE [6]), at the RHIC in AuAu collisions (STAR [7], PHENIX [8], BRAHMS [9]), and at the SPS in fixed-target experiments (NA49 [10]).

The LHCb detector [11, 12] covers the forward pseudorapidity region ($2 < \eta < 5$), as opposed to other experiments that have helium identification capabilities only at central pseudorapidity (small $|\eta|$). The LHCb experiment can therefore measure helium production in a region that is unexplored by other experiments. It is a single-arm forward spectrometer that includes a high-precision charged-particle reconstruction (tracking) system consisting of: a silicon-strip vertex detector (VELO) [13, 14] that surrounds the pp interaction region, a large-area silicon-strip detector (TT) [15] located upstream of a dipole magnet with a bending power of about 4 Tm, and three stations of silicon-strip detectors (IT) [16, 17] and straw drift tubes (OT) [18, 19] placed downstream of the magnet. The tracking system measures the momentum p of charged particles with a relative uncertainty that ranges from 0.5% at low momentum¹ to 1.0% at 200 GeV. The minimum distance of a track to a primary vertex (PV), the impact parameter (IP), is measured with a resolution of $(15+29/p_T)$ μm where p_T is the component of the momentum transverse to the beam, in GeV. Different types of charged hadrons are distinguished from one another using information from two ring-imaging Cherenkov (RICH) detectors [20, 21].

The method presented in this paper exploits information from energy losses through ionisation in the silicon sensors, alongside information from the OT and RICH to improve the separation power between helium and minimally-ionising particles of charge $Z = 1$ (bkg). It is assumed throughout this paper that all observed helium is ^3He , due to the suppression by a factor $\mathcal{O}(10^3)$ predicted by coalescence for each additional baryon [22]. A dedicated study for the ^4He production in pp collisions exploring the particle identification capabilities of the LHCb RICH is foreseen in the future.

2 Energy-loss measurements

The average energy loss per path length of a particle of charge Z passing through a silicon sensor (dE/dx) is proportional to Z^2 , as modelled by the Bethe-Bloch formula [23]. This is illustrated on the left-hand side of Fig. 1. In silicon, these energy losses are converted into around 80 electron-hole pairs per micron, and the movement of this charge in the electric field of the depleted region induces a signal on the readout strips. This signal can appear

¹Natural units where $\hbar = c = 1$ are used throughout.

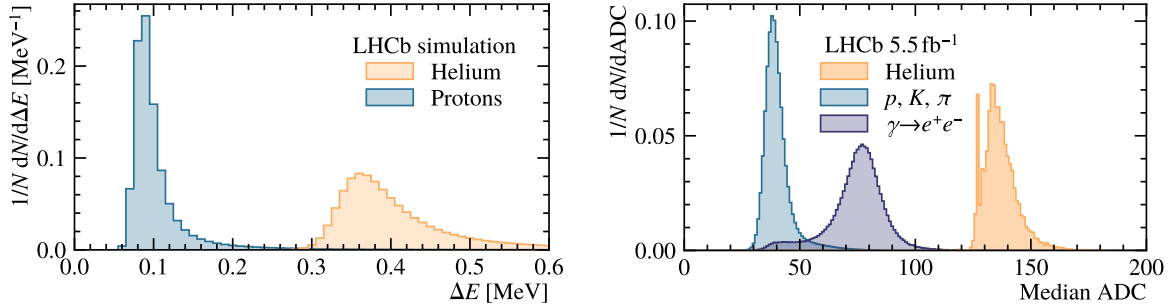


Figure 1: Left: Distributions of the deposited energy in a VELO sensor for simulated helium and protons. Right: Distributions of the median ADC of all VELO clusters per track, corrected for the incidence angle, for $Z = 1$ particles (blue), electrons from photon conversions (purple), and helium (orange). The helium selection, described in the text, is applied but no VELO requirements are imposed.

in one or a few strips, depending on the electric field, incidence angle, and couplings between strips. The strips in LHCb silicon sensors have different pitch, width, length and shapes, thus leading to different electric fields, total capacitances, and couplings. The signal from each strip is registered by the front-end electronics and measured by the readout system, which is equipped with 7-bit analogue-to-digital converters. This limits the dynamical range to 127 counts per strip, and given that one count corresponds to ~ 440 collected electrons, signals above $\sim 56\,000$ electrons saturate. Neighbouring signal strips are typically combined into a clusters of up to four strips. The counts from the strips in a cluster are summed together to obtain the cluster amplitude (ADC). The saturated strips lead to an underestimation of the cluster ADC, an effect that is partially compensated by the increasing cluster size (CLS) for $Z = 2$ particles.

The distribution of the median ADC of all clusters per track, corrected for the incidence angle, is shown on the right-hand side of Fig. 1. The sensors are calibrated such that the signal from $Z = 1$ particles peaks at $ADC \sim 40$, whilst the helium signal is found to peak at $ADC \sim 135$. This is as expected from the Z^2 dependence, taking into account saturation effects. One such effect is the sharp feature at $ADC = 127$, which corresponds to $CLS = 1$ clusters that saturate. The distribution of electrons from photon conversions is discussed in Sect. 4.3.

3 Sample selection

The results presented in this paper are obtained with the pp -collision data collected during the years 2016, 2017, and 2018, at a centre-of-mass energy $\sqrt{s} = 13$ TeV. The total integrated luminosity of 5.5 fb^{-1} is composed of 1.6 fb^{-1} collected in 2016, 1.7 fb^{-1} in 2017, and 2.2 fb^{-1} in 2018. The combined output of all LHCb physics trigger lines [24] is used. As detailed in Sect. 3.1, two data subsets, called “preselection 1” and “preselection 2”, are defined in a data reduction stage that takes place after the trigger and full data reconstruction.

In addition, minimum-bias data, recorded with random triggers, are used to study the performance of the identification method. This sample consists of 1.7×10^8 events

with 2.1×10^9 tracks. Reference samples of singly-charged particles are also obtained from $\Lambda \rightarrow p\pi^-$ and $D^{*+} \rightarrow D^0(K^-\pi^+)\pi^+$ decays² that are processed into dedicated calibration data [25]. They contain around 10^9 tracks in total and correspond to an integrated luminosity of 3 fb^{-1} .³ These samples are supplemented by kaons and pions from $B^0 \rightarrow K^{*0}(K^+\pi^-)J/\psi(\mu^+\mu^-)$ candidates selected from data corresponding to 5.5 fb^{-1} .

The response of the LHCb detector to ${}^3\text{He}$ is simulated using a simplistic Monte Carlo simulation where a single particle is generated at the nominal pp interaction point and traced through the LHCb detector using the GEANT4 toolkit [26]. The simulated events are processed by the same reconstruction software as for the data. An additional sample of simulated $B^0 \rightarrow K^{*0}(K^+\pi^-)J/\psi(\mu^+\mu^-)$ decays is used for comparison with the matching data sample.

Selected tracks are required to have passed through the VELO, TT, and the three tracking stations downstream of the magnet. A requirement is placed on the significance of the match between upstream and downstream track segments to suppress fake tracks and particles produced in interactions with the detector material. The rigidity of each track, $p/|Z|$, is required to be larger than 2.5 GV and the transverse component of the rigidity must be at least 0.3 GV. Each track must also be of good quality and have a sufficient number of hits in the silicon detectors to enable the identification techniques discussed below. Tracks that fulfil these requirements are considered well-reconstructed.

3.1 Preselection

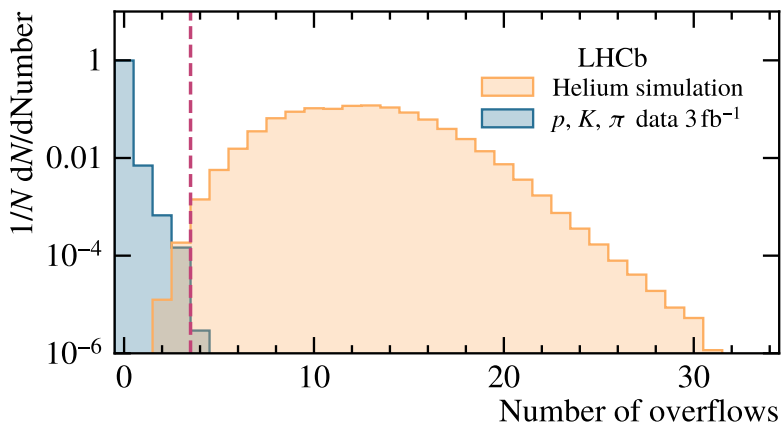


Figure 2: Distributions of the number of overflows for simulated helium signal and $Z = 1$ particles from calibration data. The vertical line indicates the preselection requirement.

In the preselection stage two simple, robust, and independent variables are used to define two subsets of data enriched in helium. Together, they ensure redundancy in the selection, and enable efficiency comparisons. The first subset, referred to as “preselection 1”, requires at least one track with the number of overflows greater than 3. This quantity is defined as the total number of saturated strips in VELO clusters along the track that have $\text{CLS} < 4$. Its distribution is shown in Fig. 2, where a clear separation between simulated helium

²The inclusion of charged-conjugate processes is implied throughout, unless otherwise stated.

³This calibration dataset only covers 2018 and part of 2017, due to missing ADC information.

and $Z = 1$ particles from calibration data is observed. The background rejection rate of this requirement is $\mathcal{O}(10^5)$. The second subset, called “preselection 2”, is obtained by requiring median ADC > 115 . Additional kinematic and track-quality requirements are applied, and pions are rejected using loose particle identification cuts. The efficiencies of these two preselections are estimated by means described in Sect. 4.1.

4 Helium identification

The VELO, IT, and TT silicon sensors have different geometries, with the most intricate one being the VELO. It has 42 modules (21 per side), each consisting of two different types of sensors with strips oriented to make measurements of the radial and azimuthal position. They are referred to as R and ϕ sensors, respectively. The TT sensors have a pitch of $183\ \mu\text{m}$ and four different strip lengths, ranging from 94 mm to 378 mm. The IT sensors that occupy the central part of the tracking stations downstream of the magnet have two different strip lengths, 108 mm and 216 mm, with $198\ \mu\text{m}$ pitch, and two different sensor thicknesses, $320\ \mu\text{m}$ and $400\ \mu\text{m}$. The thicker sensors produce larger signals. To account for different sensor geometries, VELO R and VELO ϕ sensors are considered separately, as are the thin and thick IT sensors; no significant improvement is found when considering TT sensors of different strip length.

Figure 3 shows the distribution of the cluster amplitude in VELO R sensors, separately for each cluster size, as obtained from simulated helium tracks, and $Z = 1$ particles from data. It can be seen that helium is characterised by larger CLS, peaks at larger ADC values, and more frequent saturation. The sharp features at ADC = 127, 254, 381 and 508 correspond to saturation of 1, 2, 3 and 4 strips, respectively.

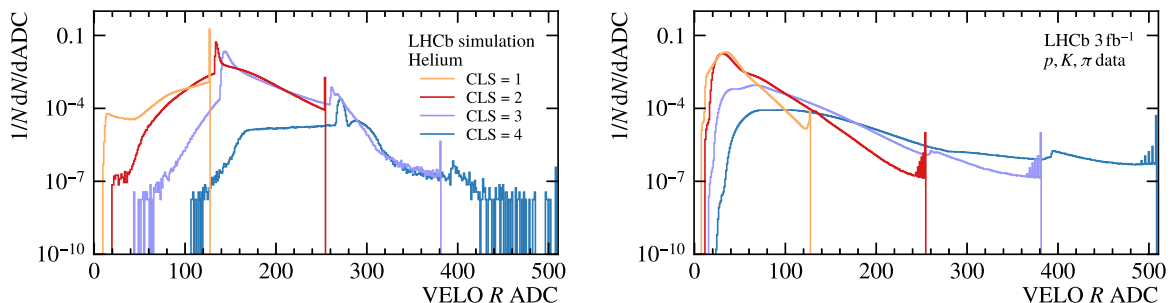


Figure 3: Distributions of the cluster amplitudes, for different cluster sizes, in the VELO R sensors for (left) simulated helium signal and (right) calibration data.

4.1 Likelihood estimators from silicon detectors

Each cluster is a separate independent measurement of the energy deposit. This information is combined into a likelihood estimator for each type of sensor. To construct this likelihood estimator, two-dimensional probability density distributions (PDD) are derived from the ADC distributions, as exemplified in Fig. 3 for VELO R sensors. One dimension of the PDD is the cluster size and the other is the ADC. To derive the likelihoods of the

helium and background particle hypotheses, the PDDs are used as look-up tables:

$$\mathcal{L}^X = \left(\prod_{i=1}^n \text{PDD}_i^X(\text{CLS}, \text{ADC}) \right)^{\frac{1}{n}}, \quad (1)$$

where $X \in \{\text{He}, \text{bkg}\}$, and n is the number of clusters on the track. Helium and background tracks are separated using the log-likelihood ratio

$$\Lambda_{\text{LD}} = \log \frac{\mathcal{L}^{\text{He}}}{\mathcal{L}^{\text{bkg}}} = \log \mathcal{L}^{\text{He}} - \log \mathcal{L}^{\text{bkg}}. \quad (2)$$

The likelihoods are evaluated for VELO R , VELO ϕ , TT, IT thick and IT thin sensors. The likelihood for the former is shown as an example in Fig. 4 on the left-hand side, where the ${}^3\text{He}$ simulation is compared to the calibration data described in Sect. 3. Significant separation power between helium and $Z = 1$ particles is observed in the likelihood estimators from all subdetectors. However, none of them would be sufficient by themselves to produce a pure helium sample from an expected helium-to-background ratio of 1 in $\mathcal{O}(10^8)$. On the right-hand side of Fig. 4, the distribution of $\Lambda_{\text{LD}}^{\text{VELO}R}$ in samples of pions and kaons from $B^0 \rightarrow K^{*0}(K^+\pi^-)J/\psi(\mu^+\mu^-)$ decays is compared between data and simulation. The shape is found to be described well by the simulation; however, the tail would lead to overestimation of the background contamination in the signal region if simulation were used for such estimates.

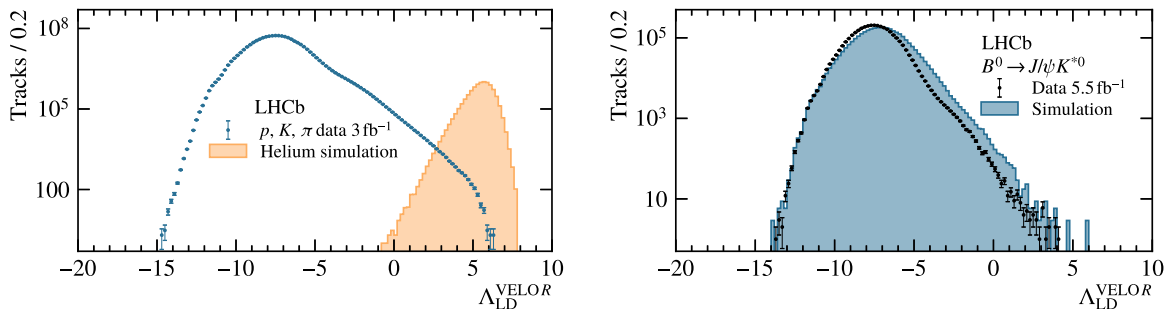


Figure 4: Distributions of $\Lambda_{\text{LD}}^{\text{VELO}R}$ in: (left) samples of $Z = 1$ tracks from calibration data and simulated helium; (right) samples of hadrons from $B^0 \rightarrow K^{*0}(K^+\pi^-)J/\psi(\mu^+\mu^-)$ decays. The simulation is normalised to the data.

For the VELO, a weighted mean of the VELO R and VELO ϕ likelihood estimators is used to define

$$\Lambda_{\text{LD}}^{\text{VELO}} = \frac{n_{\text{VELO}R} \times \Lambda_{\text{LD}}^{\text{VELO}R} + n_{\text{VELO}\phi} \times \Lambda_{\text{LD}}^{\text{VELO}\phi}}{n_{\text{VELO}R} + n_{\text{VELO}\phi}}. \quad (3)$$

The weights $n_{\text{VELO}R}$ and $n_{\text{VELO}\phi}$ are the number of clusters on the track in R and ϕ sensors, respectively. The thin and thick IT estimators are combined in the same way to obtain $\Lambda_{\text{LD}}^{\text{IT}}$.

The two-dimensional distributions of $\Lambda_{\text{LD}}^{\text{VELO}}$ versus $\Lambda_{\text{LD}}^{\text{TT}}$, and $\Lambda_{\text{LD}}^{\text{IT}}$ versus $\Lambda_{\text{LD}}^{\text{TT}}$ in minimum-bias data are presented in Fig. 5. On the left-hand side, a population of around 50 helium candidates, clearly separated from $Z = 1$ particles, is observed for

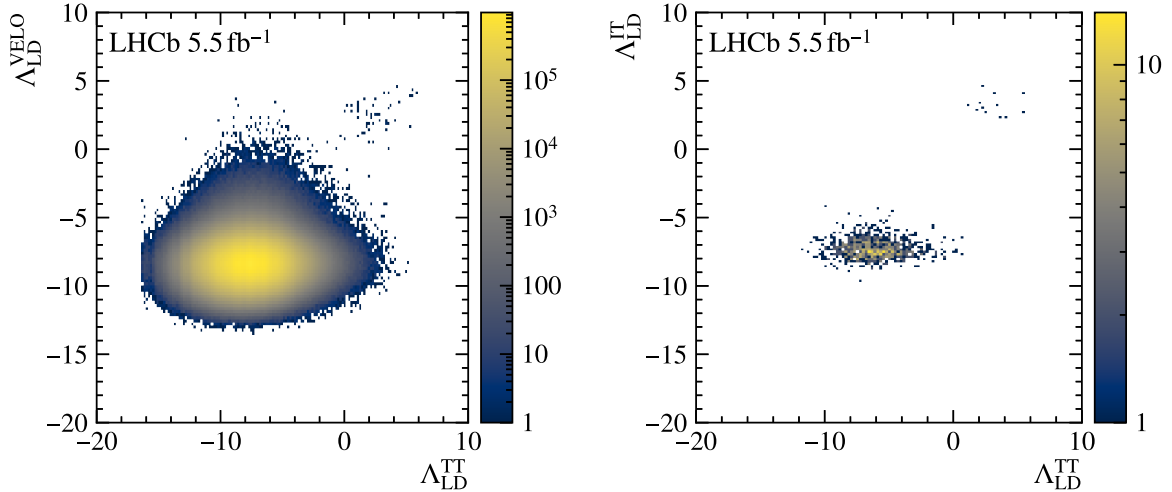


Figure 5: Distributions of the log-likelihood estimators from the LHCb VELO ($\Lambda_{\text{LD}}^{\text{VELO}}$), TT ($\Lambda_{\text{LD}}^{\text{TT}}$) and IT ($\Lambda_{\text{LD}}^{\text{IT}}$) silicon trackers from the minimum-bias data. Left: the tracks are required to pass the selection described in Sect. 4.2 or to have $\Lambda_{\text{LD}}^{\text{TT}} > -1$. Right: the tracks must traverse the IT and have $\Lambda_{\text{LD}}^{\text{VELO}} > 0$. The full selection described in Sects. 4.2, 4.3 and 5.1 is applied.

$\Lambda_{\text{LD}}^{\text{VELO}} > 0$ and $\Lambda_{\text{LD}}^{\text{TT}} > -1$. Given that there are $\mathcal{O}(10^9)$ tracks in the minimum-bias data, this indicates a separation power of at least 1 in 10^8 . Roughly $\sim 20\%$ of these tracks are in the IT acceptance and Fig. 5 (right) shows that they are predominantly distributed at large $\Lambda_{\text{LD}}^{\text{IT}}$ values.

The roughly 50 helium candidates are used to estimate the efficiencies of the two preselections discussed in Sect. 3.1. As shown on the left-hand side of Fig. 6, the overlap of the selected tracks is around 30%. In addition, both preselections are found to be approximately 50% efficient, as shown on the left-hand side of Fig. 6 for the case of preselection 1. The differences between the distribution of helium candidates and of simulated helium is attributed to imperfect modelling of the number of overflows.

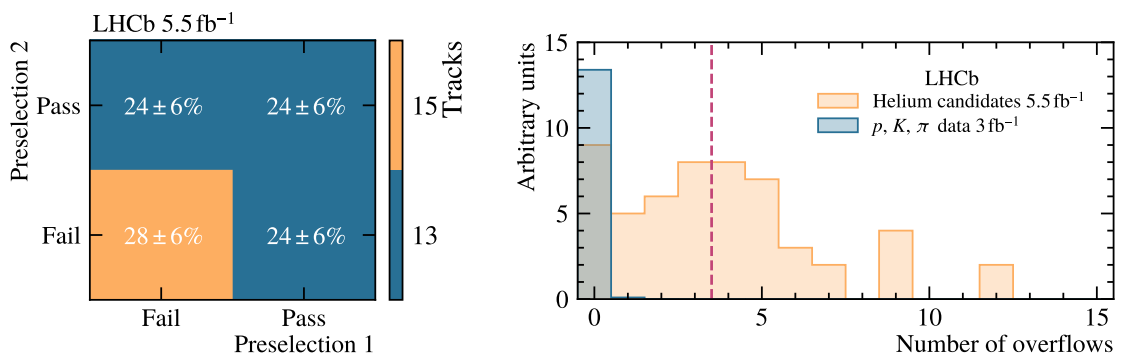


Figure 6: Left: Efficiency matrix of the two preselections determined from the helium candidates selected in minimum-bias data. Right: Distribution of the number of overflows in helium candidate tracks from minimum-bias data and $Z = 1$ particles from calibration data. The latter is normalised to 25% of the former. The requirement used in the preselection is shown in magenta.

4.2 Track-time measurements from the OT

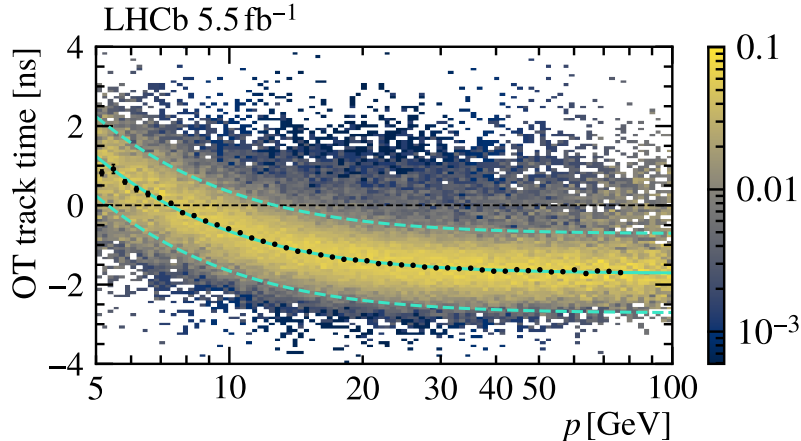


Figure 7: Distribution of the reference track time versus the momentum for tracks with $\Lambda_{\text{LD}}^{\text{VELO}} > 0$ and $\Lambda_{\text{LD}}^{\text{TT}} > 1$. In each momentum slice, the distribution is normalised to unity and fitted with a Gaussian function. The positions of the means is indicated by the black dots. These are fitted as described in the main body, resulting in the shape depicted by the green continuous line. The dotted green lines indicate the ± 1 ns interval.

The VELO and the TT stations measure the dE/dx of tracks before the magnet; however, the IT silicon detector after the magnet does not cover the full detector acceptance. The rest of the tracks are detected by the OT, which consists of gaseous drift tubes that measure the drift time of ionisation clusters produced by passing charged tracks; the time resolution is around 1 ns. The OT is calibrated such that the reference track time (t_0) is zero for $Z = 1$ particles [19]. However, helium produces on average four times more ionisation in the gas, thus triggering the readout discriminator earlier. Therefore, helium is characterised by negative t_0 values at high momentum ($p > 10$ GeV), as shown in Fig. 7. Across the entire kinematic range, the shift is influenced by the momentum dependence of dE/dx . At low momentum, the time measurement is sensitive to the mass of ^3He , leading to an upwards shift of around 4 ns at a momentum of 5 GeV.

The momentum dependence of t_0 is parameterised by a smooth function depicted in Fig. 7. This function is used to calculate the expected time of a given track (t_{fit}). As part of the selection of helium candidates, tracks passing through the OT are required to have $\Delta t_{\text{OT}} \equiv |t_0 - t_{\text{fit}}| < 1$ ns. This requirement significantly reduces the background with minimal signal loss.

The VELO and TT estimators provide helium identification upstream of the magnet. The combination of the IT and OT provides similar information downstream of the magnet, which is essential to discriminate the signal from photon conversions, as discussed in the following section.

4.3 Rejection of photon conversions

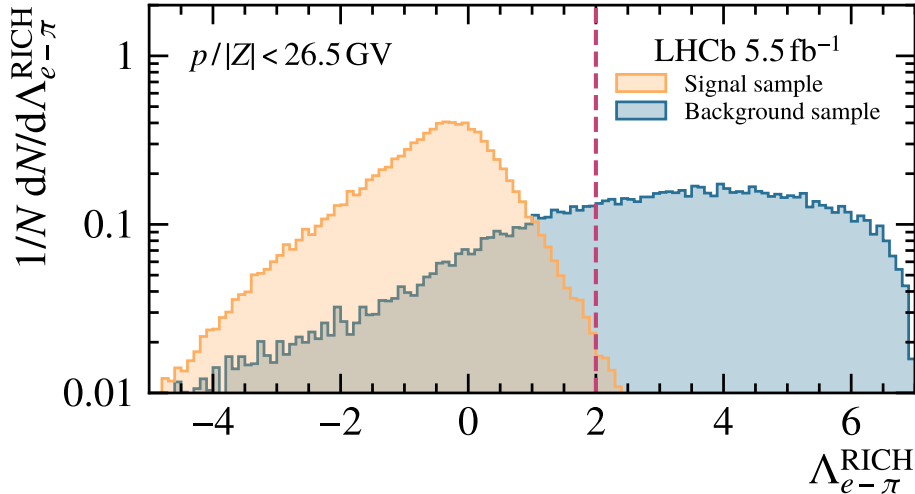


Figure 8: Distribution of the RICH electron-pion separation estimator ($\Lambda_{e-\pi}^{\text{RICH}}$) for helium signal and background below the rigidity thresholds for Cherenkov photon production by ^3He in the two LHCb RICH detectors. The vertical dashed line indicates the selection requirement.

A photon traversing the LHCb detector may produce an electron-positron pair with a small opening angle; the electron and positron may lose energy in the same silicon sensors, thus leading to a cluster whose amplitude is on average twice as large as expected from a $Z = 1$ particle, as can be seen in the right-hand-side of Fig. 1. Because of this, e^+e^- pairs from photon conversions in the VELO are not distinguished from helium as easily as other $Z = 1$ particles. The electrons and positrons are deflected in opposite directions by the magnet but the resulting distinct tracks share the same segment in the VELO. Therefore, conversions are suppressed by accepting only tracks that do not share their VELO segment with another track.

In addition, the RICH is used to construct log-likelihoods corresponding to different mass hypotheses for each track in the event. These are standard variables used in LHCb measurements, with the pion hypothesis being the default given that pions are the most produced particles.

Helium nuclei must have momenta of at least 53 GeV to produce Cherenkov rings in the RICH. Since most detected helium track candidates are below this threshold, the response of the RICH detectors to tracks in the signal sample is expected to be dominated by Cherenkov photons from other tracks in the event. However, electrons below the pion momentum threshold may be separated using the difference between the RICH log-likelihoods constructed assuming the associated track is either a pion or an electron. This quantity, denoted by $\Lambda_{e-\pi}^{\text{RICH}}$, is used to reject electrons from photon conversions, as illustrated in Fig. 8. It depicts the distributions of $\Lambda_{e-\pi}^{\text{RICH}}$ in a helium-enriched and a background-enriched sample. The former consists of tracks required to have $\Lambda_{\text{LD}}^{\text{VELO}} > 0$ and $\Lambda_{\text{LD}}^{\text{TT}} > 1$, whilst the latter comprises tracks selected using the cuts $\Lambda_{\text{LD}}^{\text{VELO}} > 0$ and $\Lambda_{\text{LD}}^{\text{TT}} < -5$. It can be seen that requiring $\Lambda_{e-\pi}^{\text{RICH}} < 2$ is expected to reject a substantial amount of background, whilst being highly efficient on the signal. The separation power is diluted at high momentum, where Cherenkov rings from helium are indistinguishable from

those produced by other particles. This low-momentum background separation technique is therefore complementary to the high-momentum one provided by the OT.

5 The helium sample

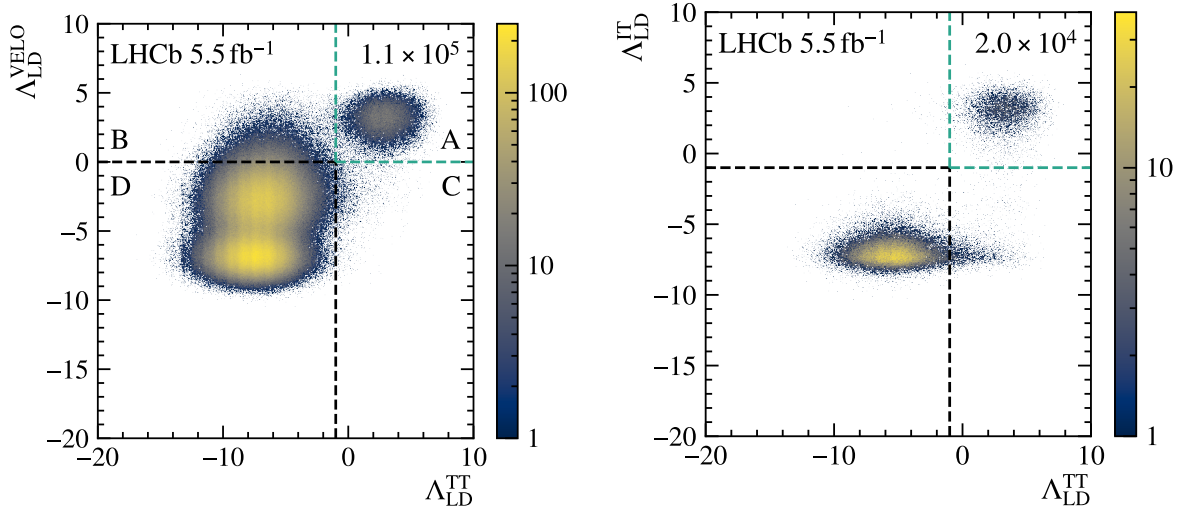


Figure 9: Distributions of the log-likelihood estimators from the LHCb VELO ($\Lambda_{LD}^{\text{VELO}}$), TT (Λ_{LD}^{TT}) and IT (Λ_{LD}^{IT}) silicon trackers. Left: the tracks are required to pass the downstream selection. Right: the tracks must traverse the IT and have $\Lambda_{LD}^{\text{VELO}} > 0$. On the left, the signal region is denoted by A, whilst regions B, C, and D correspond to background.

Table 1: Helium selection criteria quantified throughout this paper. The logical or is required between the two preselection criteria. Given the complementary acceptances of OT and IT, the logical or is also required between the downstream requirements.

Type	Track property	Selection
Acceptance, kinematics	η	$\in (2, 5)$
	$p/ Z $	$> 2.5 \text{ GV}$
	$p_T/ Z $	$> 0.3 \text{ GV}$
Preselection	Number of overflows	> 3
	Median ADC	> 115
Downstream	Δt_{OT}	$< 1 \text{ ns}$
	Λ_{LD}^{IT}	> -1
Conversion rejection	Unique VELO segment	Yes
PV origin	$\Lambda_{e-\pi}^{\text{RICH}}$	< 2
	$\ln \chi_{\text{IP}}^2$	< 2

The data selected by applying the requirements described in the previous sections are shown in Figs. 9 and 10. Additionally, tracks that are incompatible with originating from

a primary vertex are rejected by means described in the following section. The selection criteria quantified thus far are summarised in Table 1. A large, well-separated population of helium candidates is observed for $\Lambda_{LD}^{VELO} > 0$ and $\Lambda_{LD}^{TT} > -1$ (region A). Approximately 1.1×10^5 candidates are selected, and Fig. 5 shows that their location is consistent with the ~ 50 candidates found in minimum-bias data.

Singly-charged particles are located at low values of Λ_{LD}^{VELO} and Λ_{LD}^{TT} (region D). They peak at two different Λ_{LD}^{VELO} values, one for each of the preselections presented in Sect. 3.1. The median ADC requirement of preselection 2 biases the Λ_{LD}^{VELO} distribution towards larger values with respect to preselection 1. Electrons from converted photons are highly collinear in the VELO but are separated by the magnetic field. This means that they cannot be separated by Λ_{LD}^{VELO} alone, however they can be separated by Λ_{LD}^{TT} and are therefore found predominantly in region B.

The Λ_{LD}^{VELO} , Λ_{LD}^{TT} , and Λ_{LD}^{IT} estimators are expected to have a mass, a momentum and an incidence-angle dependence, due to the Bethe-Bloch formula. This is studied in detail, and is found to be barely resolvable with the 7-bit ADC resolution of the LHCb silicon trackers. As a result, the obtained distributions are continuous and nearly independent of these quantities. This is illustrated for Λ_{LD}^{VELO} in Fig. 11. The material in the LHCb detector is inhomogenously distributed in pseudorapidity and azimuthal angle, however no significant dependence of the separation power on these quantities is observed.

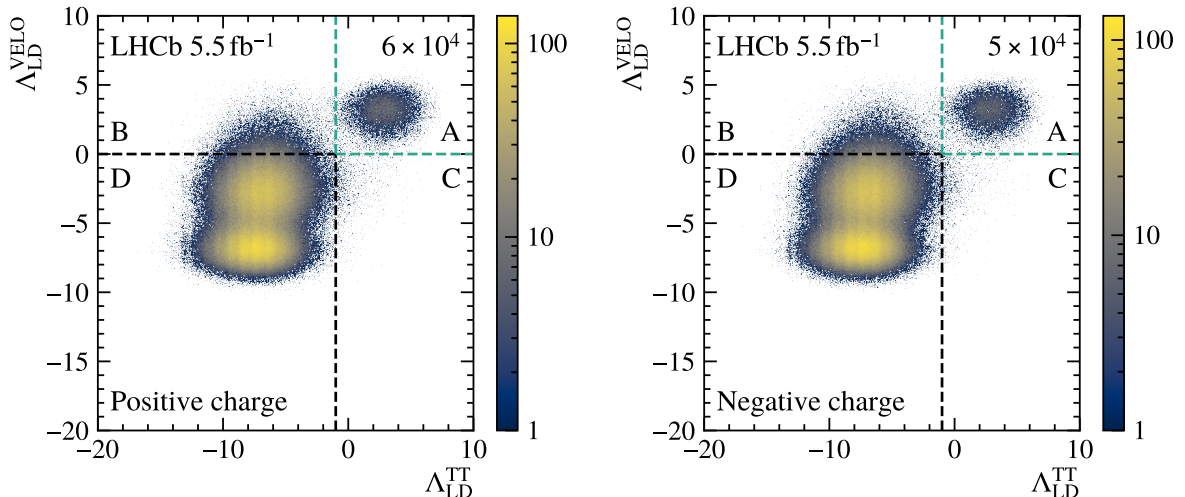


Figure 10: Distributions corresponding to that on the left-hand side of Fig. 9, but separated into tracks of (left) positive and (right) negative charge.

5.1 Helium production in the detector material

Helium nuclei, like protons, are also produced in interactions with the detector material or the beam pipe. This does not apply to antihelium, thus inducing an asymmetry in distributions of variables that are different for prompt and non-prompt particles. One such variable is the change in the χ^2 of the PV when it is reconstructed with or without the track of interest. This quantity, denoted by χ_{IP}^2 , is very close to the square of the ratio between the impact parameter of the track and its uncertainty.

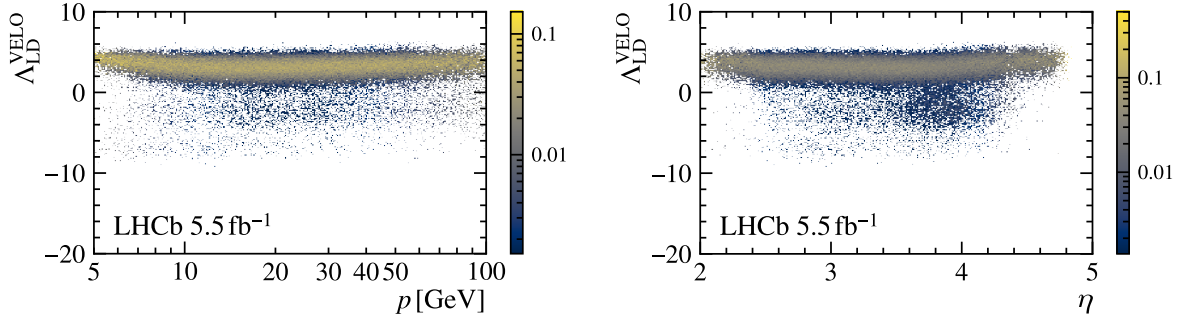


Figure 11: Distribution of Λ_{LD}^{VELO} as a function of momentum (left) and pseudorapidity (right), in data from both preselections combined. Tracks are required to pass the selection in Sect. 4.2, as well as $\Lambda_{LD}^{TT} > -1$. Each vertical slice is normalised to unity.

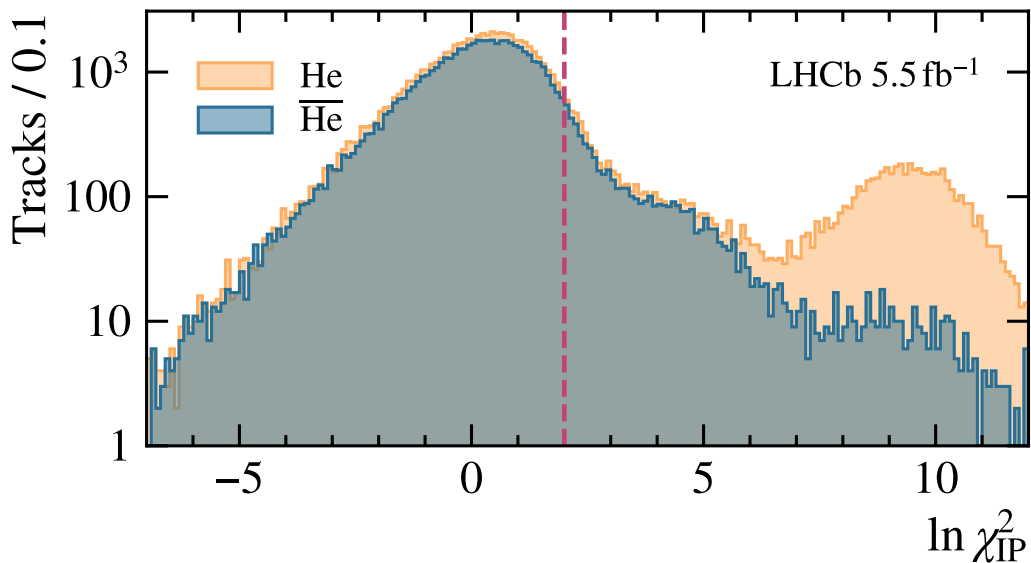


Figure 12: Distribution of the natural logarithm of the χ_{IP}^2 for helium and antihelium tracks, combining data from both preselections. The requirement that separates prompt and displaced helium is shown in red.

The distribution of $\ln \chi_{IP}^2$ in selected helium tracks is shown in Fig. 12. An enhancement is observed at large values in the helium candidate sample, but not in the antihelium one. This enhancement is consistent with the production of helium in the detector material. Therefore, prompt and displaced helium tracks are isolated by a cut on χ_{IP}^2 . The upper tail in the antihelium distribution above $\ln \chi_{IP}^2 > 2$ is a sign of non-prompt contributions to the sample, as expected from hypertriton or Λ_b^0 decays. Only tracks with $\ln \chi_{IP}^2 < 2$ are considered for the results presented throughout Sect. 5.

5.2 Estimation of residual contamination

The projections onto the Λ_{LD}^{VELO} axis of the 2D distributions displayed in Fig. 10 are used to estimate the level of residual background and are shown in Fig. 13. The distribution of

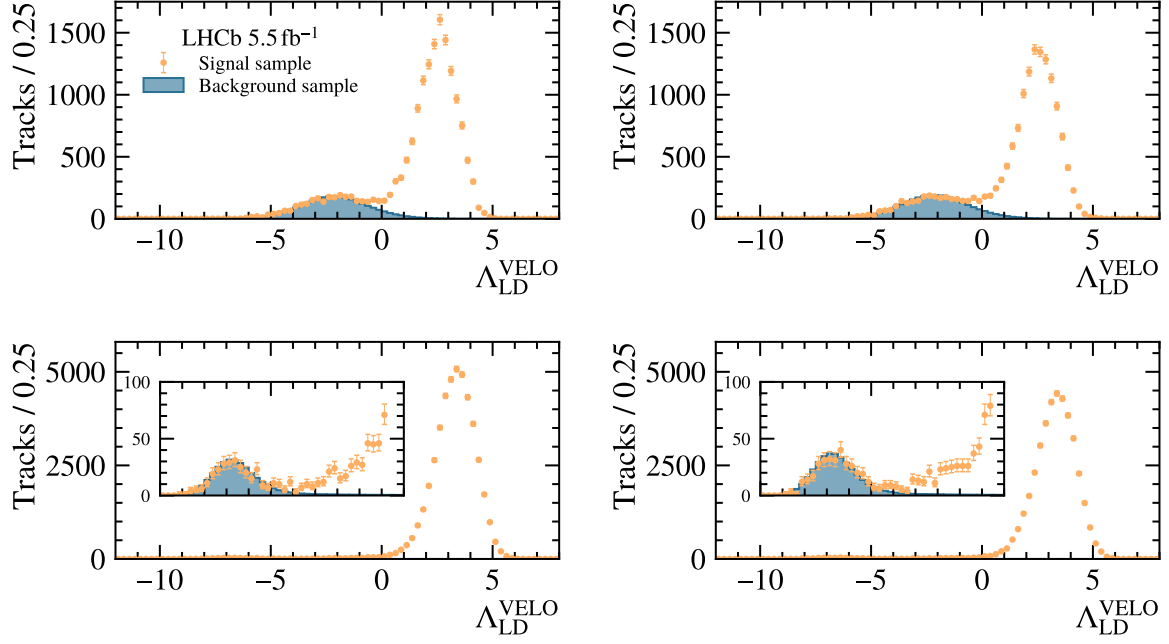


Figure 13: Distribution of $\Lambda_{LD}^{\text{VELO}}$ in (left) helium and (right) antihelium samples from the (upper) preselection 2 and (lower) preselection 1 data samples. The distribution from an independent background sample is shown in blue, scaled to match the size of the populations found in data at negative $\Lambda_{LD}^{\text{VELO}}$ values. To visualise the background in the preselection 1 sample, the inset of each bottom-row plot shows a magnification of the region $\Lambda_{LD}^{\text{VELO}} \in [-10, -1]$. Each inset's horizontal axis matches that of the containing plot.

$\Lambda_{LD}^{\text{VELO}}$ in background samples obtained from regions B and D ($\Lambda_{LD}^{\text{VELO}} < 0$) are scaled to match that in region C. The level of contamination is inferred to be the size of the tail at $\Lambda_{LD}^{\text{VELO}} > 0$.

The procedure is performed separately on the preselection 1 subset, which contains around 75% of the tracks in region A, and on data from the preselection 2 sample. This is due to the fact that the requirements for preselection 2 bias the background towards larger values, as explained in Sect. 3.1. The background sample is required to have $\Lambda_{LD}^{\text{TT}} < -2$. In the case of preselection 2, the shape of the background is shifted by +0.5 to account for correlations between Λ_{LD}^{TT} and $\Lambda_{LD}^{\text{VELO}}$, which can be seen in Fig. 9. This shift is determined by minimising the χ^2 between the signal and background histograms at negative $\Lambda_{LD}^{\text{VELO}}$ values. Fig. 13 shows that the background in the signal region, *i.e.* at $\Lambda_{LD}^{\text{VELO}} > 0$, is negligible.

The signal region of preselection 1 contains 8.7×10^4 tracks, of which 15 are expected to be background. Together with the observation of 54 helium tracks in minimum-bias, the number of background tracks in the signal region in minimum-bias that pass the same requirements can be estimated to be 6×10^{-3} . Given the total number of 1.2×10^9 well-reconstructed tracks in the minimum-bias sample, this leads to a mis-identification probability for such a background track to pass the helium identification of $\mathcal{O}(10^{-12})$.

6 Summary

Employing techniques that are almost entirely data driven, helium and antihelium are observed for the first time at the LHCb experiment. This is done using dE/dx measurements in the silicon sensors (VELO, TT and IT), alongside information from the RICH and OT subdetectors.

A total of 1.1×10^5 prompt helium and antihelium are identified with negligible background contamination in the LHCb pp collision data collected in the years 2016 to 2018. The efficiency of the helium identification method is estimated to be approximately 50% with a corresponding background rejection factor of up to $\mathcal{O}(10^{12})$.

The identification method will be applied to other LHCb Run 2 datasets, such as proton-ion, ion-ion, and SMOG collision data. Compared to the ALICE experiment, which covers the central rapidity region $|y| < 0.5$, the LHCb results will extend the available measurements in the so far experimentally unexplored forward region ($2 < \eta < 5$). This identification technique, innovative at the LHCb experiment, proves the feasibility of a rich programme of measurements of QCD and astrophysics interest involving light nuclei.

Acknowledgements





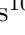
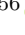


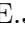

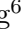





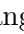





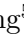
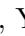


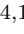


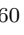

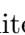
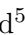



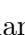



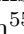



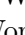
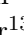
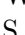

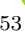

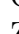
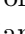

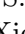





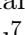


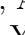

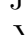
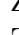
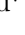


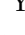

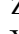
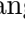

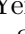


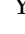

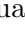

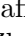

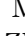
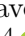
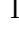
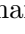

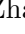

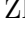


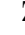
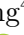

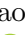

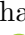

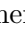

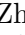
We express our gratitude to our colleagues in the CERN accelerator departments for the excellent performance of the LHC. We thank the technical and administrative staff at the LHCb institutes. We acknowledge support from CERN and from the national agencies: CAPES, CNPq, FAPERJ and FINEP (Brazil); MOST and NSFC (China); CNRS/IN2P3 (France); BMBF, DFG and MPG (Germany); INFN (Italy); NWO (Netherlands); MNiSW and NCN (Poland); MCID/IFA (Romania); MICINN (Spain); SNSF and SER (Switzerland); NASU (Ukraine); STFC (United Kingdom); DOE NP and NSF (USA). We acknowledge the computing resources that are provided by CERN, IN2P3 (France), KIT and DESY (Germany), INFN (Italy), SURF (Netherlands), PIC (Spain), GridPP (United Kingdom), CSCS (Switzerland), IFIN-HH (Romania), CBPF (Brazil), Polish WLCG (Poland) and NERSC (USA). We are indebted to the communities behind the multiple open-source software packages on which we depend. Individual groups or members have received support from ARC and ARDC (Australia); Minciencias (Colombia); AvH Foundation (Germany); EPLANET, Marie Skłodowska-Curie Actions, ERC and NextGenerationEU (European Union); A*MIDEX, ANR, IPhU and Labex P2IO, and Région Auvergne-Rhône-Alpes (France); Key Research Program of Frontier Sciences of CAS, CAS PIFI, CAS CCEPP, Fundamental Research Funds for the Central Universities, and Sci. & Tech. Program of Guangzhou (China); GVA, XuntaGal, GENCAT, Inditex, InTalent and Prog. Atracción Talento, CM (Spain); SRC (Sweden); the Leverhulme Trust, the Royal Society and UKRI (United Kingdom).

References

- [1] M. W. Winkler and T. Linden, *Dark matter annihilation can produce a detectable antihelium flux through $\bar{\Lambda}_b$ decays*, Phys. Rev. Lett. **126** (2021) 101101, arXiv:2006.16251.

- [2] S. Dupourqué, L. Tibaldo, and P. von Ballmoos, *Constraints on the antistar fraction in the Solar System neighborhood from the 10-year Fermi Large Area Telescope gamma-ray source catalog*, Phys. Rev. **D103** (2021) 083016.
- [3] AMS collaboration, M. Aguilar *et al.*, *The Alpha Magnetic Spectrometer (AMS) on the international space station: Part II — Results from the first seven years*, Phys. Rept. **894** (2021) 1.
- [4] S. Ting, *Latest results from AMS on the International Space Station*, 8 June 2023. <https://indico.cern.ch/event/1275785/>.
- [5] AMS collaboration, M. Aguilar *et al.*, *Precision measurement of the helium flux in primary cosmic rays of rigidities 1.9 GV to 3 TV with the Alpha Magnetic Spectrometer on the International Space Station*, Phys. Rev. Lett. **115** (2015) 211101.
- [6] ALICE collaboration, S. Acharya *et al.*, ${}^3\Lambda\text{H}$ and ${}^3\bar{\Lambda}\text{H}$ lifetime measurement in Pb-Pb collisions at $\sqrt{s_{\text{NN}}} = 5.02$ TeV via two-body decay, Phys. Lett. **B797** (2019) 134905, arXiv:1907.06906.
- [7] STAR collaboration, J. Adam *et al.*, *Measurement of the mass difference and the binding energy of the hypertriton and antihypertriton*, Nature Phys. **16** (2020) 409, arXiv:1904.10520.
- [8] PHENIX collaboration, S. S. Adler *et al.*, *Deuteron and antideuteron production in Au + Au collisions at $\sqrt{s_{\text{NN}}} = 200$ GeV*, Phys. Rev. Lett. **94** (2005) 122302, arXiv:nucl-ex/0406004.
- [9] BRAHMS collaboration, I. Arsene *et al.*, *Rapidity dependence of deuteron production in central Au + Au collisions at $\sqrt{s_{\text{NN}}} = 200$ GeV*, Phys. Rev. C **83** (2011) 044906, arXiv:1005.5427.
- [10] NA49 collaboration, V. I. Kolesnikov, *Production of (anti)deuterons in heavy-ion collisions at SPS energies*, PoS Baldin ISHEPP XXII (2015) 075.
- [11] LHCb collaboration, A. A. Alves Jr. *et al.*, *The LHCb detector at the LHC*, JINST **3** (2008) S08005.
- [12] LHCb collaboration, R. Aaij *et al.*, *LHCb detector performance*, Int. J. Mod. Phys. **A30** (2015) 1530022, arXiv:1412.6352.
- [13] LHCb collaboration, *LHCb VELO (Vertex Locator): Technical Design Report*, CERN-LHCC-2001-011, 2001.
- [14] R. Aaij *et al.*, *Performance of the LHCb Vertex Locator*, JINST **9** (2014) P09007, arXiv:1405.7808.
- [15] LHCb collaboration, *LHCb reoptimized detector design and performance: Technical Design Report*, CERN-LHCC-2003-030, 2003.
- [16] R. Arink *et al.*, *Performance of the LHCb Outer Tracker*, JINST **9** (2014) P01002, arXiv:1311.3893.

- [17] LHCb collaboration, *LHCb inner tracker: Technical Design Report*, CERN-LHCC-2002-029, 2002.
- [18] LHCb collaboration, *LHCb outer tracker: Technical Design Report*, CERN-LHCC-2001-024, 2001.
- [19] P. d'Argent *et al.*, *Improved performance of the LHCb Outer Tracker in LHC Run 2*, JINST **12** (2017) P11016, arXiv:1708.00819.
- [20] M. Adinolfi *et al.*, *Performance of the LHCb RICH detector at the LHC*, Eur. Phys. J. **C73** (2013) 2431, arXiv:1211.6759.
- [21] R. Calabrese *et al.*, *Performance of the LHCb RICH detectors during LHC Run 2*, JINST **17** (2022) P07013, arXiv:2205.13400.
- [22] ALICE collaboration, S. Acharya *et al.*, *Production of deuterons, tritons, ^3He nuclei and their antinuclei in pp collisions at $\sqrt{s} = 0.9, 2.76$ and 7 TeV*, Phys. Rev. **C97** (2018) 024615, arXiv:1709.08522.
- [23] Particle Data Group, R. L. Workman *et al.*, *Review of particle physics*, Prog. Theor. Exp. Phys. **2022** (2022) 083C01.
- [24] R. Aaij *et al.*, *Performance of the LHCb trigger and full real-time reconstruction in Run 2 of the LHC*, JINST **14** (2019) P04013, arXiv:1812.10790.
- [25] R. Aaij *et al.*, *Selection and processing of calibration samples to measure the particle identification performance of the LHCb experiment in Run 2*, EPJ Tech. Instrum. **6** (2019) 1, arXiv:1803.00824.
- [26] Geant4 collaboration, J. Allison *et al.*, *Geant4 developments and applications*, IEEE Trans. Nucl. Sci. **53** (2006) 270; Geant4 collaboration, S. Agostinelli *et al.*, *Geant4: A simulation toolkit*, Nucl. Instrum. Meth. **A506** (2003) 250.

D. vom Bruch¹² , V. Vorobyev⁴¹ , N. Voropaev⁴¹ , K. Vos⁷⁶ , G. Vouters¹⁰ , C. Vrahas⁵⁶ , J. Walsh³² , E.J. Walton¹ , G. Wan⁶ , C. Wang¹⁹ , G. Wang⁸ , J. Wang⁶ , J. Wang⁵ , J. Wang⁴ , J. Wang⁷¹ , M. Wang²⁷ , N. W. Wang⁷ , R. Wang⁵² , X. Wang⁶⁹ , X. W. Wang⁵⁹ , Y. Wang⁸ , Z. Wang¹³ , Z. Wang⁴ , Z. Wang⁷ , J.A. Ward^{54,1} , N.K. Watson⁵¹ , D. Websdale⁵⁹ , Y. Wei⁶ , B.D.C. Westhenry⁵² , D.J. White⁶⁰ , M. Whitehead⁵⁷ , A.R. Wiederhold⁵⁴ , D. Wiedner¹⁷ , G. Wilkinson⁶¹ , M.K. Wilkinson⁶³ , M. Williams⁶² , M.R.J. Williams⁵⁶ , R. Williams⁵³ , F.F. Wilson⁵⁵ , W. Wislicki³⁹ , M. Witek³⁸ , L. Witola¹⁹ , C.P. Wong⁶⁵ , G. Wormser¹³ , S.A. Wotton⁵³ , H. Wu⁶⁶ , J. Wu⁸ , Y. Wu⁶ , K. Wyllie⁴⁶ , S. Xian⁶⁹ , Z. Xiang⁵ , Y. Xie⁸ , A. Xu³² , J. Xu⁷ , L. Xu⁴ , L. Xu⁴ , M. Xu⁵⁴ , Z. Xu¹¹ , Z. Xu⁷ , Z. Xu⁵ , D. Yang⁴ , S. Yang⁷ , X. Yang⁶ , Y. Yang^{26,L} , Z. Yang⁶ , Z. Yang⁶⁴ , V. Yeroshenko¹³ , H. Yeung⁶⁰ , H. Yin⁸ , C. Y. Yu⁶ , J. Yu⁶⁸ , X. Yuan⁵ , E. Zaffaroni⁴⁷ , M. Zavertyaev¹⁸ , M. Zdybal³⁸ , M. Zeng⁴ , C. Zhang⁶ , D. Zhang⁸ , J. Zhang⁷ , L. Zhang⁴ , S. Zhang⁶⁸ , S. Zhang⁶ , Y. Zhang⁶ , Y. Zhang⁶¹ , Y. Z. Zhang⁴ , Y. Zhao¹⁹ , A. Zharkova⁴¹ , A. Zhelezov¹⁹ , X. Z. Zheng⁴ , Y. Zheng⁷ , T. Zhou⁶ , X. Zhou⁸ , Y. Zhou⁷ , V. Zhovkovska⁵⁴ , L. Z. Zhu⁷ , X. Zhu⁴ , X. Zhu⁸ , Z. Zhu⁷ , V. Zhukov^{16,41} , J. Zhuo⁴⁵ , Q. Zou^{5,7} , D. Zuliani³⁰ , G. Zunica⁶⁰ .

¹*School of Physics and Astronomy, Monash University, Melbourne, Australia*

²*Centro Brasileiro de Pesquisas Físicas (CBPF), Rio de Janeiro, Brazil*

³*Universidade Federal do Rio de Janeiro (UFRJ), Rio de Janeiro, Brazil*

⁴*Center for High Energy Physics, Tsinghua University, Beijing, China*

⁵*Institute Of High Energy Physics (IHEP), Beijing, China*

⁶*School of Physics State Key Laboratory of Nuclear Physics and Technology, Peking University, Beijing, China*

⁷*University of Chinese Academy of Sciences, Beijing, China*

⁸*Institute of Particle Physics, Central China Normal University, Wuhan, Hubei, China*

⁹*Consejo Nacional de Rectores (CONARE), San Jose, Costa Rica*

¹⁰*Université Savoie Mont Blanc, CNRS, IN2P3-LAPP, Annecy, France*

¹¹*Université Clermont Auvergne, CNRS/IN2P3, LPC, Clermont-Ferrand, France*

¹²*Aix Marseille Univ, CNRS/IN2P3, CPPM, Marseille, France*

¹³*Université Paris-Saclay, CNRS/IN2P3, IJCLab, Orsay, France*

¹⁴*Laboratoire Leprince-Ringuet, CNRS/IN2P3, Ecole Polytechnique, Institut Polytechnique de Paris, Palaiseau, France*

¹⁵*LPNHE, Sorbonne Université, Paris Diderot Sorbonne Paris Cité, CNRS/IN2P3, Paris, France*

¹⁶*I. Physikalisches Institut, RWTH Aachen University, Aachen, Germany*

¹⁷*Fakultät Physik, Technische Universität Dortmund, Dortmund, Germany*

¹⁸*Max-Planck-Institut für Kernphysik (MPIK), Heidelberg, Germany*

¹⁹*Physikalisches Institut, Ruprecht-Karls-Universität Heidelberg, Heidelberg, Germany*

²⁰*School of Physics, University College Dublin, Dublin, Ireland*

²¹*INFN Sezione di Bari, Bari, Italy*

²²*INFN Sezione di Bologna, Bologna, Italy*

²³*INFN Sezione di Ferrara, Ferrara, Italy*

²⁴*INFN Sezione di Firenze, Firenze, Italy*

²⁵*INFN Laboratori Nazionali di Frascati, Frascati, Italy*

²⁶*INFN Sezione di Genova, Genova, Italy*

²⁷*INFN Sezione di Milano, Milano, Italy*

²⁸*INFN Sezione di Milano-Bicocca, Milano, Italy*

²⁹*INFN Sezione di Cagliari, Monserrato, Italy*

³⁰*Università degli Studi di Padova, Università e INFN, Padova, Padova, Italy*

³¹*INFN Sezione di Perugia, Perugia, Italy*

³²*INFN Sezione di Pisa, Pisa, Italy*

³³*INFN Sezione di Roma La Sapienza, Roma, Italy*

- ³⁴ INFN Sezione di Roma Tor Vergata, Roma, Italy
- ³⁵ Nikhef National Institute for Subatomic Physics, Amsterdam, Netherlands
- ³⁶ Nikhef National Institute for Subatomic Physics and VU University Amsterdam, Amsterdam, Netherlands
- ³⁷ AGH - University of Science and Technology, Faculty of Physics and Applied Computer Science, Kraków, Poland
- ³⁸ Henryk Niewodniczanski Institute of Nuclear Physics Polish Academy of Sciences, Kraków, Poland
- ³⁹ National Center for Nuclear Research (NCBJ), Warsaw, Poland
- ⁴⁰ Horia Hulubei National Institute of Physics and Nuclear Engineering, Bucharest-Magurele, Romania
- ⁴¹ Affiliated with an institute covered by a cooperation agreement with CERN
- ⁴² DS4DS, La Salle, Universitat Ramon Llull, Barcelona, Spain
- ⁴³ ICCUB, Universitat de Barcelona, Barcelona, Spain
- ⁴⁴ Instituto Galego de Física de Altas Enerxías (IGFAE), Universidade de Santiago de Compostela, Santiago de Compostela, Spain
- ⁴⁵ Instituto de Física Corpuscular, Centro Mixto Universidad de Valencia - CSIC, Valencia, Spain
- ⁴⁶ European Organization for Nuclear Research (CERN), Geneva, Switzerland
- ⁴⁷ Institute of Physics, Ecole Polytechnique Fédérale de Lausanne (EPFL), Lausanne, Switzerland
- ⁴⁸ Physik-Institut, Universität Zürich, Zürich, Switzerland
- ⁴⁹ NSC Kharkiv Institute of Physics and Technology (NSC KIPT), Kharkiv, Ukraine
- ⁵⁰ Institute for Nuclear Research of the National Academy of Sciences (KINR), Kyiv, Ukraine
- ⁵¹ University of Birmingham, Birmingham, United Kingdom
- ⁵² H.H. Wills Physics Laboratory, University of Bristol, Bristol, United Kingdom
- ⁵³ Cavendish Laboratory, University of Cambridge, Cambridge, United Kingdom
- ⁵⁴ Department of Physics, University of Warwick, Coventry, United Kingdom
- ⁵⁵ STFC Rutherford Appleton Laboratory, Didcot, United Kingdom
- ⁵⁶ School of Physics and Astronomy, University of Edinburgh, Edinburgh, United Kingdom
- ⁵⁷ School of Physics and Astronomy, University of Glasgow, Glasgow, United Kingdom
- ⁵⁸ Oliver Lodge Laboratory, University of Liverpool, Liverpool, United Kingdom
- ⁵⁹ Imperial College London, London, United Kingdom
- ⁶⁰ Department of Physics and Astronomy, University of Manchester, Manchester, United Kingdom
- ⁶¹ Department of Physics, University of Oxford, Oxford, United Kingdom
- ⁶² Massachusetts Institute of Technology, Cambridge, MA, United States
- ⁶³ University of Cincinnati, Cincinnati, OH, United States
- ⁶⁴ University of Maryland, College Park, MD, United States
- ⁶⁵ Los Alamos National Laboratory (LANL), Los Alamos, NM, United States
- ⁶⁶ Syracuse University, Syracuse, NY, United States
- ⁶⁷ Pontifícia Universidade Católica do Rio de Janeiro (PUC-Rio), Rio de Janeiro, Brazil, associated to ³
- ⁶⁸ School of Physics and Electronics, Hunan University, Changsha City, China, associated to ⁸
- ⁶⁹ Guangdong Provincial Key Laboratory of Nuclear Science, Guangdong-Hong Kong Joint Laboratory of Quantum Matter, Institute of Quantum Matter, South China Normal University, Guangzhou, China, associated to ⁴
- ⁷⁰ Lanzhou University, Lanzhou, China, associated to ⁵
- ⁷¹ School of Physics and Technology, Wuhan University, Wuhan, China, associated to ⁴
- ⁷² Departamento de Física, Universidad Nacional de Colombia, Bogota, Colombia, associated to ¹⁵
- ⁷³ Universität Bonn - Helmholtz-Institut für Strahlen und Kernphysik, Bonn, Germany, associated to ¹⁹
- ⁷⁴ Eotvos Lorand University, Budapest, Hungary, associated to ⁴⁶
- ⁷⁵ Van Swinderen Institute, University of Groningen, Groningen, Netherlands, associated to ³⁵
- ⁷⁶ Universiteit Maastricht, Maastricht, Netherlands, associated to ³⁵
- ⁷⁷ Tadeusz Kosciuszko Cracow University of Technology, Cracow, Poland, associated to ³⁸
- ⁷⁸ Department of Physics and Astronomy, Uppsala University, Uppsala, Sweden, associated to ⁵⁷
- ⁷⁹ University of Michigan, Ann Arbor, MI, United States, associated to ⁶⁶
- ⁸⁰ Departement de Physique Nucleaire (SPhN), Gif-Sur-Yvette, France

^a Universidade de Brasília, Brasília, Brazil

^b Centro Federal de Educação Tecnológica Celso Suckow da Fonseca, Rio De Janeiro, Brazil

^c Hangzhou Institute for Advanced Study, UCAS, Hangzhou, China

^d LIP6, Sorbonne Université, Paris, France

- ^e *Excellence Cluster ORIGINS, Munich, Germany*
- ^f *Universidad Nacional Autónoma de Honduras, Tegucigalpa, Honduras*
- ^g *Università di Bari, Bari, Italy*
- ^h *Università di Bologna, Bologna, Italy*
- ⁱ *Università di Cagliari, Cagliari, Italy*
- ^j *Università di Ferrara, Ferrara, Italy*
- ^k *Università di Firenze, Firenze, Italy*
- ^l *Università di Genova, Genova, Italy*
- ^m *Università degli Studi di Milano, Milano, Italy*
- ⁿ *Università di Milano Bicocca, Milano, Italy*
- ^o *Università di Padova, Padova, Italy*
- ^p *Università di Perugia, Perugia, Italy*
- ^q *Scuola Normale Superiore, Pisa, Italy*
- ^r *Università di Pisa, Pisa, Italy*
- ^s *Università della Basilicata, Potenza, Italy*
- ^t *Università di Roma Tor Vergata, Roma, Italy*
- ^u *Università di Siena, Siena, Italy*
- ^v *Università di Urbino, Urbino, Italy*
- ^w *Universidad de Alcalá, Alcalá de Henares, Spain*
- ^x *Universidade da Coruña, Coruña, Spain*
- ^y *Department of Physics/Division of Particle Physics, Lund, Sweden*
- [†] *Deceased*